

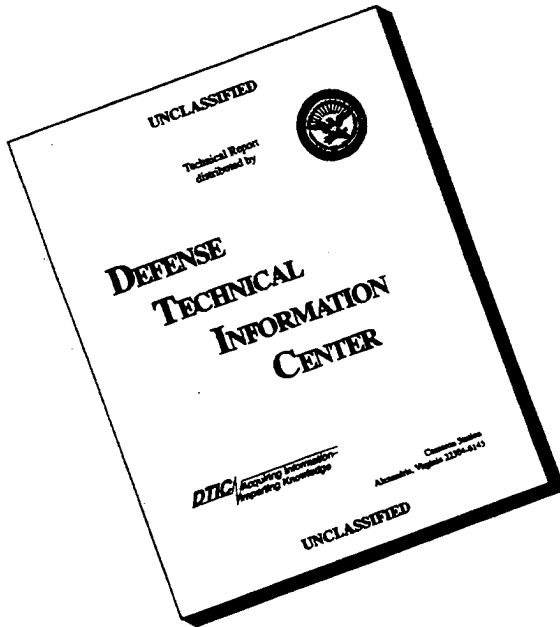
## REPORT DOCUMENTATION PAGE

Form Approved  
OMB No. 0704-0188

Public reporting burden for this collection of information is estimated to average 1 hour per response, including the time for reviewing instructions, searching existing data sources, gathering and maintaining the data needed, and completing and reviewing the collection of information. Send comments regarding this burden estimate or any other aspect of this collection of information, including suggestions for reducing this burden, to Washington Headquarters Services, Directorate for Information Operations and Reports, 1215 Jefferson Davis Highway, Suite 1204, Arlington, VA 22202-4302, and to the Office of Management and Budget, Paperwork Reduction Project (0704-0188), Washington, DC 20503.

1. AGENCY USE ONLY (Leave blank)	2. REPORT DATE	3. REPORT TYPE AND DATES COVERED	
	April 10, 1995	Final Technical Rpt: 9/15/91-9/14/94	
4. TITLE AND SUBTITLE		5. FUNDING NUMBERS	
Matrix and Interface Deformation in High Temperature Intermetallic Compounds and Composites			
6. AUTHOR(S)		AFOSR-91-0427	
R.J. Asaro			
7. PERFORMING ORGANIZATION NAME(S) AND ADDRESS(ES)		8. PERFORMING ORGANIZATION	
University of California, San Diego Department of AMES, 0411 La Jolla, CA 92093		AFOSR-TR-96 0078	
9. SPONSORING/MONITORING AGENCY NAME(S) AND ADDRESS(ES)		AGENCY REPORT NUMBER	
Dr. C.H. Ward Air Force Office of Scientific Research/NE, Bldg. 410, Rm 219 Bolling Air Force Base Washington, D.C. 20332-6448			
11. SUPPLEMENTARY NOTES			
12a. DISTRIBUTION/AVAILABILITY STATEMENT		12b. DISTRIBUTION CODE	
Dr. C.H. Ward  <div style="border: 1px solid black; padding: 5px; text-align: center;">Approved for public release; Distribution Unlimited</div>			
13. ABSTRACT (Maximum 200 words)			
<p>This project is concerned with the experimental and theoretical study of deformation and fracture mechanisms in MoSi<sub>2</sub> and TiAl alloy materials and of interfaces between these alloys. Past work has included 1) identifying dominant deformation mechanisms in MoSi<sub>2</sub>, 2) predicting the geometric hardening for suggested slip systems in MoSi<sub>2</sub>, and 3) finite element simulations of the deformation in intermetallic compounds (TiAl, MoSi<sub>2</sub>) pertaining to the microstructural subtleties in polycrystalline aggregates. More recent work has been concerned with the modeling of lamella microstructures in Ti<sub>3</sub>Al/TiAl and TiAl alloys. In particular, the framework has been created to perform detailed modeling of deformation processing in TiAl alloys.</p> <p style="text-align: right;">19960321 078</p>			
14. SUBJECT TERMS		15. NUMBER OF PAGES 22	
		16. PRICE CODE	
17. SECURITY CLASSIFICATION OF REPORT UNCLASSIFIED	18. SECURITY CLASSIFICATION OF THIS PAGE UNCLASSIFIED	19. SECURITY CLASSIFICATION OF ABSTRACT UNCLASSIFIED	20. LIMITATION OF ABSTRACT UL

# **DISCLAIMER NOTICE**



**THIS DOCUMENT IS BEST  
QUALITY AVAILABLE. THE  
COPY FURNISHED TO DTIC  
CONTAINED A SIGNIFICANT  
NUMBER OF PAGES WHICH DO  
NOT REPRODUCE LEGIBLY.**

## Abstract

This report briefly elucidates the progress made during the course of research undertaken under AFOSR grant no: 91-0427. The thrust of this work involves deformation modeling, identification of dominant contributors to plasticity, and exploring the subtleties of microstructural effects in brittle intermetallics Molybdenum Disilicide and Titanium Aluminides and are described under separate headings.

**A. Molybdenum Disilicide:** Experimental evidence of stacking faults in MoSi<sub>2</sub>, processed over a range of solidification velocities is presented. Shear type faults are observed on {110} planes in plasma-sprayed polycrystalline specimens (grown at 10<sup>6</sup>cm/hr growth rate). Condensation faults on (001) planes, probably associated with silicon loss during processing, are observed in single crystals (grown at 1cm/hr to 30cm/hr growth rates) and are thermally stable. Prior experimental evidence for the transformation of C40-MoSi<sub>2</sub> (high temperature phase) to C11<sub>b</sub>-MoSi<sub>2</sub> (low temperature phase) has been re-evaluated such that the fault character, and in particular the existence of the C40 structure, is questioned. Thus, transformation-induced stacking faults, originally described as 1/4<111> lying on {110} have been reinterpreted as 1/6[001] condensation faults on (001). The possibility of these faults contributing to strain (under the action of diffusion-assisted mechanisms) and strain-hardening (by crystallographic glide processes) is elucidated.

Deformation Modeling efforts assuming crystallographic slip indicate that finite deformation textures could only be produced by <100>{013} slip and not by <111>{110} slip. Additionally, such textures could also be produced by fracturing effects on (001).

**B. Titanium Aluminides:** Tensile Deformation microstructures in  $\gamma$ -TiAl +  $\alpha_2$ Ti<sub>3</sub>Al based fully lamellar (FL) and nearly lamellar (NL) microstructures have been simulated using micro-mechanical methods. The deformation is extremely inhomogenous resulting in a large accumulation of hydrostatic stresses at the grain boundaries, thereby promoting intergranular fracture initiation. In particular, the increase in ductility with increasing equiaxed  $\gamma$ -grain volume fraction (with compliant deformation characteristics) in nearly lamellar alloys is explained by the reduction of the hydrostatic stress buildup at the boundaries, consequently mitigating fracture.

For finite deformations in compression, crystals with their lamella parallel to the loading axis, demonstrate an increased tendency to buckling and contribute to localized behavior extensively.

## A) Molybdenum Disilicide

Research efforts were directed in two broad categories: i) Establishing the dominant deformation mechanisms responsible for the observed high temperature plastic behavior in MoSi<sub>2</sub>, ii) Exploring the textural effects of activating the different proposed slip systems in MoSi<sub>2</sub>

### i. Dominant High Temperature Deformation Mechanisms in MoSi<sub>2</sub>

We are attempting to explore the deformation contributions of the various slip systems being proposed (as observed in transmission electron microscopy (TEM) investigations) in the literature. Several aspects of the high temperature ductile behavior are of interest; i) the plastic behavior is extremely strain rate sensitive (Gibala, Ghosh, Van Aken, Srolovitz, Basu, Chang, Mason and Yang, 1992), suggesting the possibility of time dependent phenomena, ii) there is significant evidence of climb dominated <100> segments lying in non-slip planes (Unal, Petrovic, Carter and Mitchell, 1990) and iii) there may be some contributions from transformation-induced plasticity (Umakoshi, Sakagami, Hirano and Yamane, 1990). The first two aspects relate to the diffusion based mechanisms, consistent with the strain rate sensitivity as observed experimentally (Gibala et. al., 1992). The latter pertains to the polymorphic transformation of the low temperature phase C11<sub>b</sub>-MoSi<sub>2</sub> to the high temperature phase C40-MoSi<sub>2</sub> (Umakoshi, Sakagami, Yamane and Hirano, 1989) presumably under applied stress.

Recently, it has been suggested that high temperature ductility can be derived from the high temperature instability (starting around 1300K) of the C11<sub>b</sub> structure with respect to the C40 structure, see figure 1. Indeed evidence of such transformation has been presented by Umakoshi, Sakagami, Yamane and Hirano (1989) in single crystals of MoSi<sub>2</sub> deformed at 1173K. It is suggested that the transformation from C11<sub>b</sub> to C40 activates 1/4<111> partial dislocations and creates pure stacking faults in MoSi<sub>2</sub>, thereby enhancing ductility. The evidence of such transformations has been questioned recently because in equilibrium phase diagram studies of high purity MoSi<sub>2</sub>, the high temperature phase field has not been detected. In particular, phase equilibrium studies (Boettinger, Perepezko and Frankwicz, 1992) preclude the possibility of an equilibrium C40->C11<sub>b</sub> polymorphic transition in pure MoSi<sub>2</sub>.

In light of these inconsistencies, we have revisited the problem of transformation-induced ductility as originally suggested. Prior experimental data has been reinterpreted, such that the fault stability, and the existence of the C40 structure is questioned. Specifically, the metastability arguments have been explored to account for the shear polymorphic transformation.

### Fault Analysis of the Transformation Evidence

The experimentally obtained contrast (Umakoshi, Sakagami, Yamane and Hirano, 1989) for the fault ( $R_F$ ) and the partial ( $b_p$ ) is presented in table 1 along with the  $g \cdot R_F$ ,  $g \cdot b_p$  tabulations for the diffracting vectors used in the analysis. The image recorded with  $g=1\bar{1}0$  offers the clearest invisibility for the bounding partial as well as the stacking fault. Thus, the choice of stacking fault partial is either 1/4[111] or 1/4[111]. In each case, the dislocation partial visibility and the fault contrast is not matched consistently for the remaining diffracting conditions. For the presumed scenario of the bounding partial, at least three images should reveal no fault contrast (i.e.,  $g \cdot R_F = 0$ , integer) whereas only one invisibility has been presented. We have also included the computed contrast for  $b_p=1/n[001]$  ( $n=1/2, 1/6$ ) which appears consistent with the experimental contrast.

Table 1: Fault Analysis of experimental data extracted from Umakoshi, Sakagami, Yamane and Hirano(1989). The six diffracting conditions are listed as presented in the published literature along with the 'computed' and 'experimental' fault contrast. The experimental data has a perfect match with  $1/2[001]$  or  $1/6[001]$  rather than the suggested  $1/4<111>$ .

$g \cdot R_F$	$1/4[111]$	$1/4[1\bar{1}\bar{1}]$	$1/2[001]$	$1/6[1\bar{1}0]$	experimental Fault	Partial
(T03)	1/2	1	V	V	V	V
(1T0)	0	0	I	I	I	I
(211)	0	-1/2	V	V	V	V
(0T3)	1/2	-1	V	V	V	V
(002)	1/2	-1/2	V	V	?	V
(2T3)	0	-1/2	V	V	V	V

It is unlikely that these errors can be attributed to rotation calibrations, since the expected fault contrast in itself does not agree with the experimental observations. Interestingly if we consider the possibility of a  $1/2[001]$  or  $1/6[001]$  partial dragging a fault, we note that the experimental contrast can be matched correctly to the computed contrast assuming the  $\mathbf{g} \cdot \mathbf{b}_p = 0$  criteria. The [001] fault can be created by shear in any plane ( $hk0$ ) and by condensation on (001).

### Experimental Evidence for New Interpretations

Our experimental evidence was obtained from i) plasma sprayed polycrystalline material produced at growth rates  $> 10^6 \text{ cm.hr}^{-1}$ , and ii) single crystal  $\text{MoSi}_2$  melt processed, in a halogen-powered optical float zone at a growth rate  $= 1.0 \text{ cm hr}^{-1}$ , in an identical fashion as that reported by Umakoshi et. al (1989,1990).

i) Plasma-sprayed material: The most significant and unique feature of the as spray-deposited specimens is the observation of a wide variety of symmetrical shear faults lying on  $\{1\bar{1}0\}$  planes. prior observation of such faults has been linked to ductility. Figure 1 shows selected micrographs of the experimentally observed contrast for the faults. Fault A exhibits a  $\mathbf{g} \cdot \mathbf{R}_F = 0$ , integer and  $\mathbf{g} \cdot \mathbf{b}_p = 0$  type for  $\mathbf{g} = 1\bar{1}0$ , figure 1(b), yielding a fault vector  $= 1/2[001]$ . This is consistent with the image formed with  $\mathbf{g} = 006$ , figure 1(c), where the partials are observed but the fault disappears on account of  $\mathbf{g} \cdot \mathbf{b}_p \neq 0$  and  $\mathbf{g} \cdot \mathbf{R}_F = \text{integer}$ , respectively. Fault B exhibits a  $\mathbf{g} \cdot \mathbf{R}_F = \text{integer}$  and  $\mathbf{g} \cdot \mathbf{b}_p = 0$  type of contrast for  $\mathbf{g} = 103$ , figure 1(a) and  $\mathbf{g} = 1\bar{1}0$ , figure 1(b), yielding a fault vector  $= 1/4[33\bar{1}]$ . Table 1 lists the contrast observations for visible (V) and invisible (I) for the fault vector ( $\mathbf{R}_F$ ) and the bounding partials ( $\mathbf{b}_p$ ) along with the expected contrast for faulted pairs of different feasible magnitudes. A  $1/6[33\bar{1}]$  fault is ruled out because of the strong contrast (see also Table 1) observed for  $\mathbf{g} = 103$ , figure 1(d), and  $\mathbf{g} = 00\bar{6}$ , figure 1(c). A  $1/3[001]$  fault is ruled out because of the strong fault contrast observed for  $\mathbf{g} = 103$ , figure 1(a), and  $\mathbf{g} = T03$ , figure 1(d). Thus, the experimentally observed contrast is consistent with fault vectors of  $1/4[33\bar{1}]$  and  $1/2[001]$  bounded by equivalent partial dislocations on either side with Burgers vectors given as  $\mathbf{b} = 1/4[33\bar{1}]$  and  $\mathbf{b} = 1/2[001]$  respectively. These dissociations are not faulted dipoles as has been confirmed by  $\pm \mathbf{g}$  analysis.

ii) Single Crystal  $\text{MoSi}_2$ : Stacking faults were readily observed in the as-grown samples as shown in figure 2. Both the stacking fault and the bounding partial are visible for  $\mathbf{g} = 0\bar{1}3$ , figure 2(a), and  $\mathbf{g} = T03$ , figure 2(b). The stacking fault exhibits a  $\mathbf{g} \cdot \mathbf{R}_F = 0$  or integer type of

Table 2. Comparison of experimentally obtained fault (F) and partial (P) contrast with the absolute values of the expected contrast for faulted pairs of varying magnitudes. The experimentally observed contrast\* is listed as visible (V) and invisible (I).

<u><math>g \cdot R_F</math></u>	[33T]*	1/4[33T]	1/6[33T]	[001]*	1/2[001]	1/3[001]
	F/P				F/P	
(T10)	I/I	0	0	I/I	0	0
(005)	V/V	3/2	1	I/V	3	2
(013)	I/I	0	0	V/V	3/2	1
(200)	V/V	3/2	1	I/I	0	0
(T03)	V/V	3/2	1	V/V	3/2	1
(T10)	V/V	3/2	1	I/I	0	0

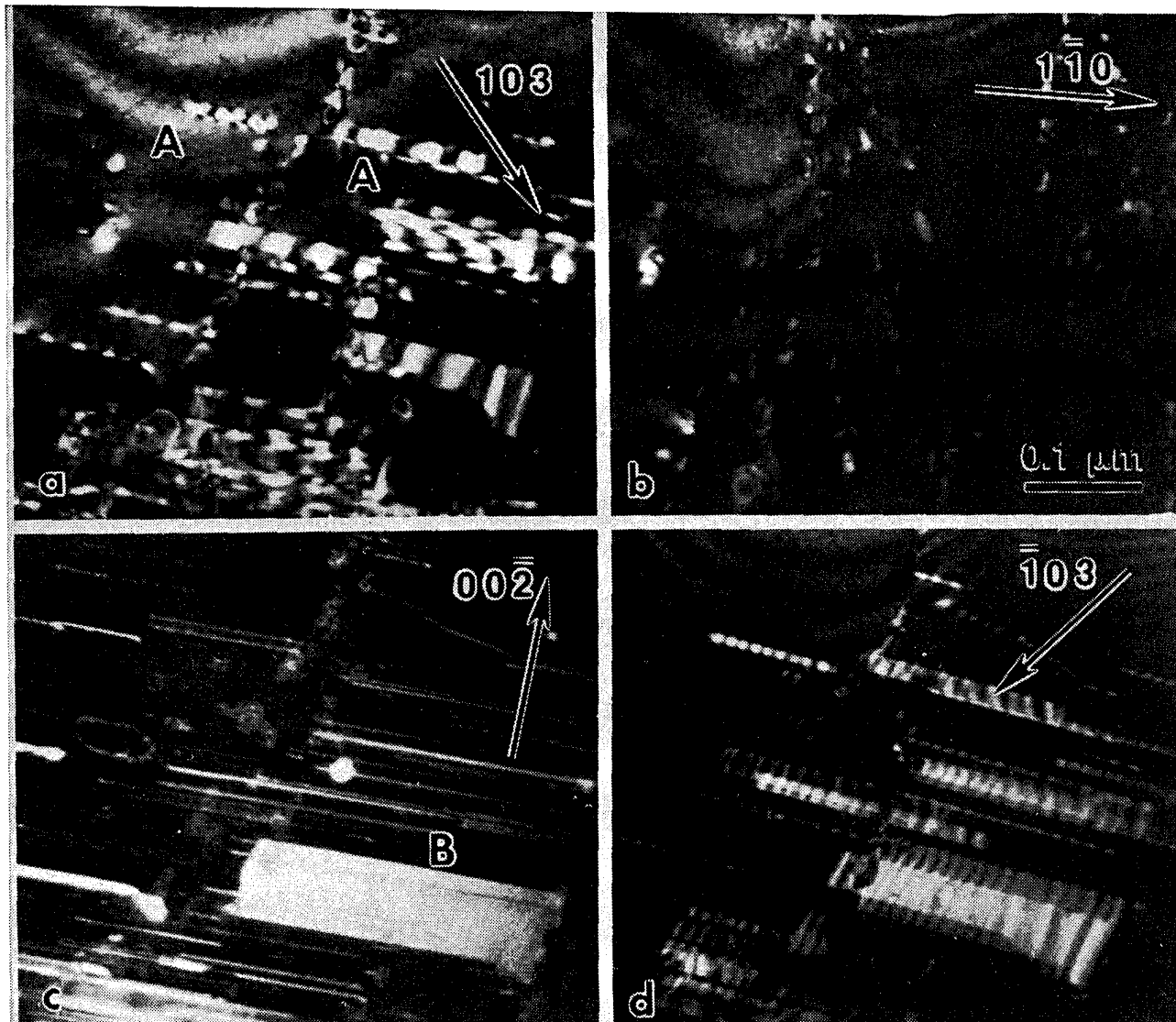


Figure 1. Weak Beam TEM micrographs of faulted partials in rapidly solidified (Spray-deposited)  $\text{MoSi}_2$ . a)  $g = 103$ ,  $B \approx [010]$ , b)  $g = 1\bar{1}0$ ,  $B \approx [110]$ , c)  $g = 00\bar{5}$ ,  $B \approx [010]$ , d)  $g = \bar{1}03$ ,  $B \approx [010]$ . Fault labeled A is dissociated as  $[001](1\bar{1}0) = 1/2[001](1\bar{1}0) + 1/2[001](\bar{1}\bar{1}0)$  and fault labeled B is dissociated as  $1/2[33\bar{T}](1\bar{1}0) = 1/4[33\bar{T}](1\bar{1}0) + 1/4[33\bar{T}](\bar{1}\bar{1}0)$ .

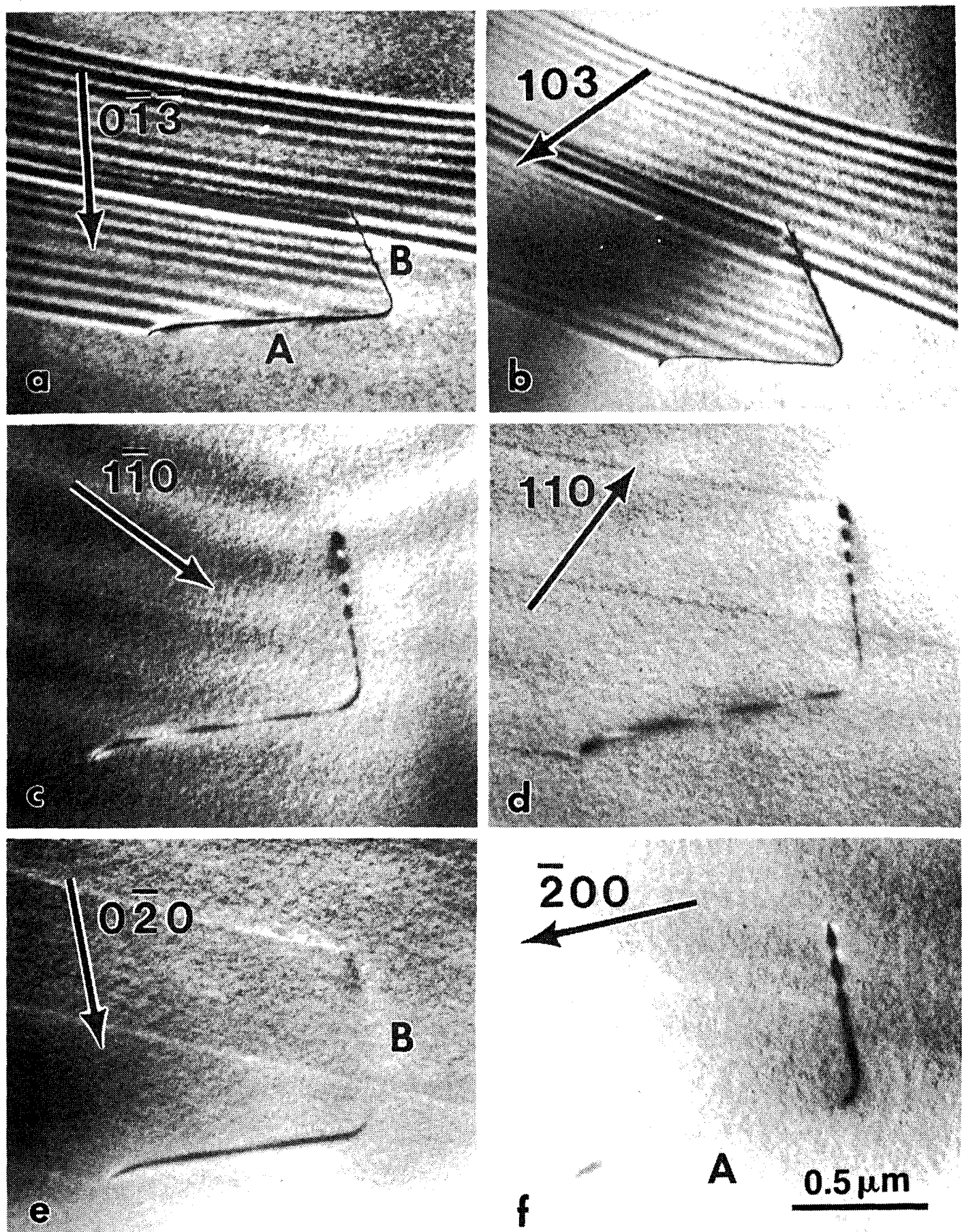


Figure 2. BFTEM micrographs of  $1/6[001]$  condensation faults on (001). a)  $g = \bar{1}03$ ,  $B \approx [3\bar{3}1]$ , b)  $g = 1\bar{1}0$ ,  $B \approx [001]$ , c)  $g = 110$ ,  $B \approx [001]$ , d)  $g = 0\bar{2}0$ ,  $B \approx [001]$ , e)  $g = \bar{2}00$ ,  $B \approx [001]$

contrast for  $\mathbf{g}=1\bar{1}0$ , figure 2(c),  $\mathbf{g}=110$ , figure 2(d),  $\mathbf{g}=0\bar{2}0$ , figure 2(e), and  $\mathbf{g}=\bar{2}00$  figure 2(f), thus yielding an  $\mathbf{R}_f=1/n[001]$ . The partial exhibits a  $\mathbf{g}\cdot\mathbf{b}=0$  and  $\mathbf{g}\cdot\mathbf{b} \times \mathbf{u} \neq 0$  type of contrast for  $\mathbf{g}=1\bar{1}0$ , figure 2(c),  $\mathbf{g}=110$ , figure 2(d),  $\mathbf{g}=0\bar{2}0$ , figure 2(e), and  $\mathbf{g}=\bar{2}00$  figure 2(f). Trace analysis indicates that the fault is spread out on the (001) plane with the line directions ( $\mathbf{u}_i$ ) of the curved partial as  $A=100$  and  $B=010$ . Thus, both A and B exhibit a  $\mathbf{g}\cdot\mathbf{b}\mathbf{x}\mathbf{u}=0$  type of contrast for  $\mathbf{g}=\bar{2}00$ , figure 2(f), and  $\mathbf{g}=0\bar{2}0$ , figure 2(e), respectively. Conventional dark field imaging indicates that the experimental contrast could not be derived from completely overlapping faults.

### Comparison with Prior Literature

For the case of single crystal data, the contrast observations of [001] faults in the present study are essentially similar to  $1/4<111>$  shear fault evidence presented earlier by Umakoshi et. al. (1989) for deformed specimens of single crystal  $\text{MoSi}_2$ . It is speculated that the condensation faults are produced possibly by i) a condensation of vacancies, or ii) by loss of silicon from the  $\text{MoSi}_2$  unit cell. The former possibility is somewhat diminished as we have observed no condensation faults in rapidly quenched specimens. Regarding the latter possibility, the idea of silicon loss is plausible, since the observation of such faults is linked with the sample's high temperature excursion during processing and/or mechanical testing. Considering the stacking in the C direction in the (LT)  $\text{C}11_b$  structure; six different layers, 2-Mo layers and 4-Si layers constitute the unit cell. The layers are stacked in sequence as Si, Si, Mo, Si, Si, Mo layers, Figure 3.

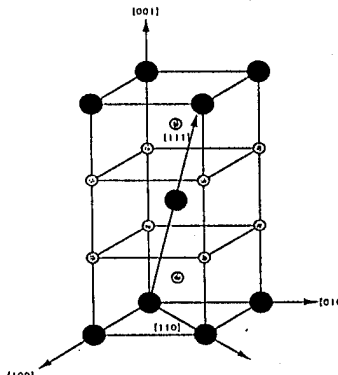


Figure 3:  $\text{MoSi}_2$  unit cell

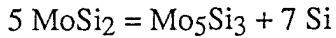
Since there are alternate sheets of Mo and Si atoms on the (001) planes in the  $\text{C}11_b$  structure, the chemistry can be altered by eliminating either the Mo sheets or Si sheets of atoms.  $\text{MoSi}_2$  is a line compound and owes its oxidation resistance to the formation of a surface film of  $\text{SiO}_2$ . One can imagine that loss of silicon, (or Mo enrichment to form  $\text{Mo}_5\text{Si}_3$ ) occurs by the removal of sheets of silicon. It is hypothesized that a single or double layer of silicon atoms may be removed to create the  $1/6[001]$  and  $1/3[001]$  fault, respectively. A  $1/3[001]$  fault is ruled out because of the strong fault contrast observed for  $\mathbf{g}=0\bar{1}3$ , figure 2(a), and  $\mathbf{g}=103$ , figure 2(b), and so a  $1/6[001]$  vector is most likely. Note that a  $1/2[001]$  fault will remove Si and Mo atoms in the ratio of 2:1, and thus no chemical changes are created.

It appears that the origin of these faults is derived specifically from the duration of the high temperature excursion. The degree to which silicon is lost depends on the processing conditions: ambient pressure, temperature of the melt, and overall time of melting (Lograsso, 1992). Thus all other things being equal, the growth velocity determines the residence time at high temperature. If temperature alone were the dominant effect, the growth velocity would not be expected to have any effect. To validate this point, single crystal samples were processed at various growth rates ranging from 1cm/hr to 30cm/r. At high growth rates no faults are observed, whereas [001] condensation faults are observed

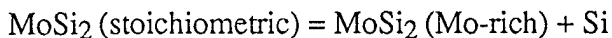
for slow growth rates indicating that their origin is somehow derived from the time dependent excursion into the high temperature regime. In this regard the suggestion of silicon loss appears most plausible. Additionally, any vacancy condensation effects are eliminated since one would expect them to be more dominant at the higher growth velocities. No specific details of the growth velocity for the optical float zone processed MoSi<sub>2</sub> crystals were presented by Umakoshi et. al. (1989), but growth rates associated with such halogen-powered optical float zone furnaces are usually low (Kimura, Nakamura and Hirano, 1990).

### Phase Diagram Implications

In the immediate vicinity of the condensation fault, with the removal of a layer of silicon atoms (see figure 1), the local chemistry is enriched from MoSi<sub>2</sub> to MoSi, such that the average unit cell now has the composition Mo<sub>2</sub>Si<sub>3</sub>. In the most recent compilation of the Mo-Si phase diagram (Massalski, 1990), MoSi<sub>2</sub> is referred to as a line compound. Thus, silicon loss to form the oxidation barrier SiO<sub>2</sub> is presumed to be derived by the decomposition reaction:



This appears plausible as Mo<sub>5</sub>Si<sub>3</sub> precipitates are routinely observed in MoSi<sub>2</sub>. Evidence of condensation faults, on the other hand, allows for a possible deviation in chemistry while retaining the C11<sub>b</sub> structure, and thus the strict definition of the 'line' compound is violated. Additionally, since condensation faults continue to grow, under the application of stress, further Mo-rich variations are likely. In the current context, the silicon loss may be accommodated by extending the phase composition of line compound MoSi<sub>2</sub> to the Mo-rich side at high temperatures, such that the reaction



may be possible. Such a possibility has indeed been indicated in an earlier version of the Mo-Si phase diagram reported by Brewer and Lamoreux (1980), as well as in the isothermal section of the Mo-Cr-Si phase diagram at 1300°C (Ageev, 1964). However, it is emphasized that: i) the changes in chemistry do not involve any 'incorrect' site occupancy, and ii) such a compositional window can only be proposed for high temperatures, presumably even greater than 1300°C, since all attempts to create such faults by heat treatment in the temperature range 1400-1600°C were unsuccessful.

### Ductility Considerations

We now attempt to explain the possible growth mechanism of such condensation loops as observed by Umakoshi et al (1989) under compressive loading. These pre-existing faults may grow upon testing in the creep regime based on diffusion-assisted climb arguments. Groves and Kelly (1969) have shown that shape changes can be produced by climb. Thus, the fault could possibly expand on the (001) plane and produce strain. Such climb would be activated by a component of stress acting normal to the plane of the fault (001). Seemingly, this explains why the faults would grow when tested in the [001] orientation. In fact, this is likely since the major contributors to deformation, the <100> dislocations, are not activated at this orientation. However, two additional facts are of related significance: i) the originally suggested mobility of 1/4<111> contributes four slip systems with strain contributions available in the  $\varepsilon_{xx}$ ,  $\varepsilon_{yy}$ ,  $\varepsilon_{zz}$  orthogonal directions, whereas the climb-assisted expansion of the [001] loops can only produce strain in the  $\varepsilon_{zz}$  direction. Thus, its role can be of minimal contribution at best. ii) we expect that these faults are significant barriers to dislocations with Burgers vectors not contained in the (001) plane because the periodicity of the lattice will introduce some APB components, as

discussed in the next section. We expect this to be of some significance as [001] is not the most likely plane for <100] slip. This point is elaborated in the next section.

### Hardening Mechanisms Introduced by Faults

Interactions of slip dislocations with various metastable and stable faults can contribute work hardening effects. As mentioned earlier, condensation faults are quite large (several microns wide), and presumably grow under the application of stress (Umakoshi, Sakagami, Hirano and Yamane, 1989). Thus the probability of their interaction with climb and or glide events is increased. For the climb event of a <100] dislocation, normal to the fault, the dislocation spreads out in the (001) plane of the fault (Kad et. al, 1995). For crystallographic glide events, the schematic diagram in Figure 4 shows the effect of  $1/2<111>$  and/or  $1/2<331>$  dislocations gliding on {110} past the (001) plane of the fault. Each event creates two layers of APB related stacking error residing on {110}, which doubles with the passage of the next dislocation. Similarly  $1/2<331>$  dislocations gliding on {013} create two layers of APB-induced stacking error on {013}. Though the APB energy on {110} is not known, it is expected to be much higher than the SISF energy  $\approx 255\text{mJ/m}^2$  (Evans, Court, Hazzledine and Fraser, 1993). Our initial flow stress results in [001] orientation, though preliminary, indicate that float zone crystals exhibit a significantly higher flow stress compared to Czochralski crystals. This flow stress behavior, also observed by Maloy, Mitchell and Heuer (1994), may be attributed to the possible effects of stable condensation faults.

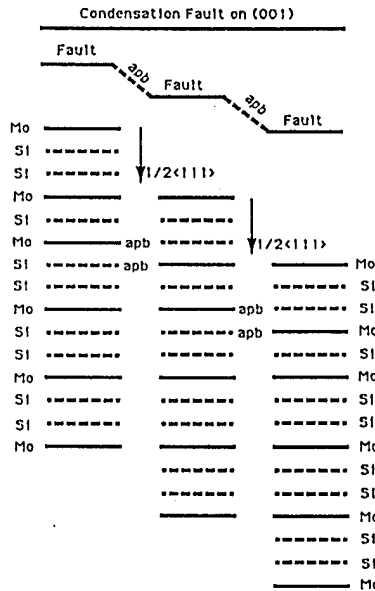


Figure 4. Schematic diagram of the hardening process as produced by the intersection of glissile dislocations, containing the 'c' component, with the condensation faults on (001). Passage of each lattice dislocation gliding on {110} planes creates an APB component on the glide plane.

### ii. Texture Effects of High Temperature Deformation

This component of research attempts to rank the proposed slip systems in  $\text{MoSi}_2$ . At least five different slip systems have been proposed in the literature. These are <100]<013>, <100]<011>, <110]<111>,  $1/4<111>\{110\}$ ,  $1/2<331>\{1100\}$ , and  $1/2<331>\{013\}$  slip systems. While they have certainly been observed in the deformed samples by TEM, it is not entirely clear if they are indeed contributing to strain or if they are just sessile residuals. This point is ever so important in brittle  $\text{MoSi}_2$ , where the mere observation in TEM

samples may in fact point to their immobile nature. To counteract this problem we are attempting to simulate the crystal rotations incurred by polycrystalline aggregates with the activation of one or a combination of slip systems. The objective of computing the geometric hardening incurred by the activation of a specific slip system is to ascertain the increasing levels of stress required to accommodate the diminishing schmid factor obtained as a result of rotation of the crystal lattice.

In the C11<sub>b</sub> structure MoSi<sub>2</sub>, the close packed slip planes (in decreasing order) are {110} and {013} with a packing density of 1.73 and 1.55 atoms per unit area ( $a^2$ , where  $a=3.2\text{\AA}$ ) respectively. The corresponding numbers for just the Mo atoms are 0.58 and 0.52, respectively. The most likely slip vectors in these close packed slip planes in MoSi<sub>2</sub> are <100>{013} and /12<111>{110}. Experimental corroborations for dominant slip system activity were obtained by compressing MoSi<sub>2</sub> compacts to strains greater than 50% in compression. Assuming random texture in the samples initially, deformation texture were measured by X-ray pole figure examinations and compared with simulations for each of the slip systems. Thus we have employed each family of slip systems (4 in each case) independently (in computationally derived deformation simulations) to generate a moderate deformation ( $\approx 0.5$  true strain). Figures 5(a) - (d) show the computed (001) texture for crystallographic slip activation for <331>{110}, 1/2<111>{110}, <100>{013}, and 1/2<331>{013} slip systems respectively.

Analysis of experimental textures presented here, Figure 6, indicate that a strong [001] fiber texture is produced parallel to the compression direction. These results can be reconciled with theoretical simulations only for the case of <100>{013}, and <331>{013} slip systems (both of which produce closely related [001] fiber textures). One additional possibility is that the brittle intermetallic undergoes some form of textural reorganization by a combination of fracture and healing processes on the (001) plane. This could account for the experimental textures observed, since any fracture process on (001) plane introduces identical rotational components (as those of <100>{013} and <331>{013} slip) necessary for texture and can be most readily reconciled with the experimental data.

These textural observations lead us to conclude that 1/2<111> dislocations reported in the literature are only minor contributors to the overall finite deformation. It seems likely that the abundant <111> dislocations observed experimentally are mere dissociations of <331> dislocations given as:

$$1/2<331> = 1/2<111> + [110],$$

where the [110] dislocations may further dissociate as

$$[110] = [100] + [010]$$

This explanation is most consistent with both the macroscopic texture alignment and microscopic dislocation observations.

## Summary

Metastable shear type faults are observed lying on {110} planes in plasma-sprayed polycrystalline specimens (grown at  $10^6\text{cm.hr}^{-1}$  growth rate). Condensation faults on (001) planes are observed in single crystals (grown at  $1\text{cm.hr}^{-1}$  growth rates) which are thermally stable. The transformational evidence presented earlier in the literature has been reinterpreted as simple condensation faults probably produced by the loss of silicon at high temperatures during crystal growth. While these faults may produce some strain by climb assisted mechanisms at high temperature, it appears that they act as general barriers to the motion of more mobile dislocation segments.

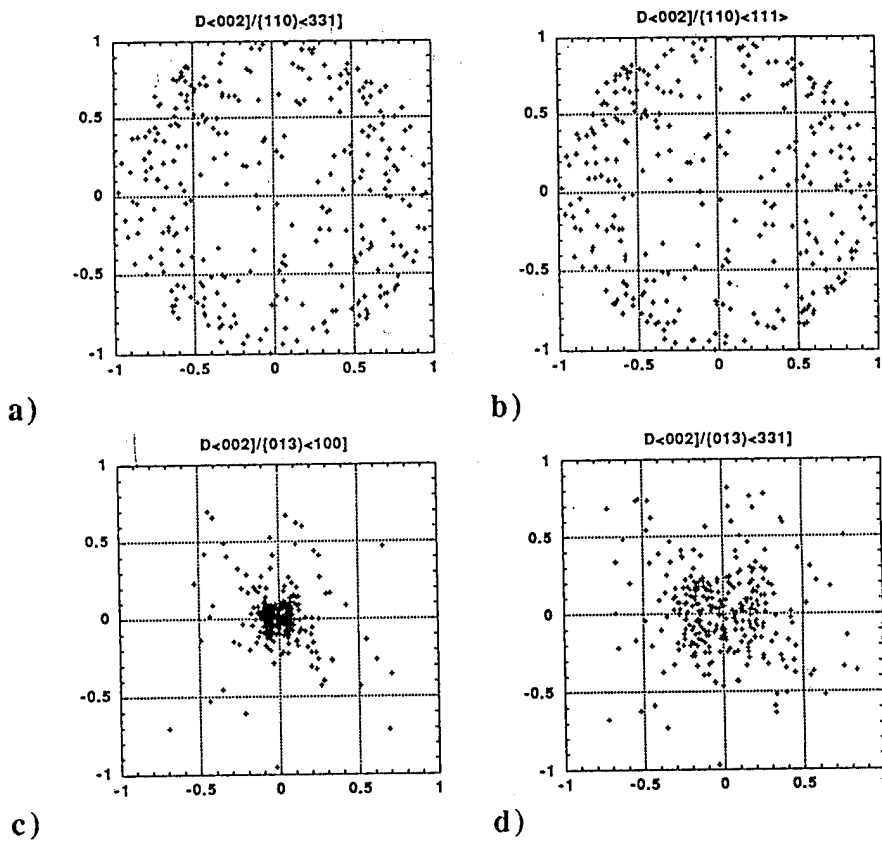


Figure 5: Simulated (001) pole figures for compression textures in MoSi<sub>2</sub> ( $\epsilon=0.6$ ) for a)  $<331>\{110\}$ , b)  $1/2<111>\{110\}$ , c)  $<100>\{013\}$ , and d)  $1/2<331>\{013\}$  slip systems respectively.

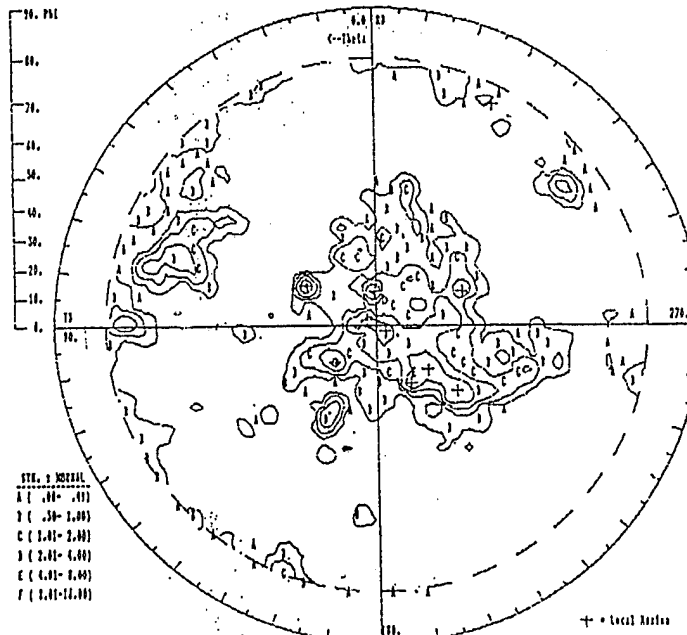


Figure 6: Experimental textures of polycrystalline MoSi<sub>2</sub> specimens deformed at 1400°C at a strain rate of  $10^{-3}$  sec<sup>-1</sup>. The textures indicate the typical [001] fiber textures produced parallel to the loading direction.

For finite compressive deformations (i.e.,  $\varepsilon \approx 0.6$ ) at high temperatures, the deformation texture can only be reconciled with  $<100\{013\}$ , and  $<331\{013\}$  slip system activation (both of which produce closely related [001] fiber textures). Additionally, it is possible that these textures are also influenced by cracking on the (001) plane, since this process could also account for the experimentally observed texture.

## References

- AGEEV, N. V. Diagrammy Sostoianija Metallicheskikh Sistem, **10**, (edited by Ageev, N.V.) Viniti Press, Moscow 1964, 182.
- BOETTINGER, W.J., PEREPEZKO, J.H. and FRANKWICZ, P.S., 1992, Mat. Sci. & Eng., **A155**, 33.
- BREWER, L. and LAMOREUX, R.H., Atomic Energy Review, Spec. Issue #7 (Molybdenum: Physico-Chemical Properties of its Compounds and Alloys), L. Brewer (ed.), Int. Atomic Energy Agency, Vienna 1980, 320.
- CASTRO, R.G., SMITH, R.W., ROLLETT, A.D. and STANEK, P., 1992, Mat. Sci & Eng., **A155**, 101.
- EVANS, D.J., COURT, S.A., HAZZLEDINE, P.M. and FRASER, H.L., 1993, Philos. Mag. Lett., **67**, 331.
- GIBALA, R., GHOSH, A. K., VAN AKEN, D. C., SROLOVITZ, D. J., BASU, A., MASON, D. P., and YANG, W., 1992, Mat. Sci & Eng., **A155**, 147.
- GROVES, G.W., and KELLY, A., 1969, Philos. Mag., **19**, 977.
- KAD, B.K., VECCHIO, K.S., and ASARO. R.J., 1993, MRS Symp. Proc., **288**, 1123.
- KIMURA, K., NAKAMURA, M. and HIRANO, T., 1990, Mat. Sci & Eng., **25**, 2487.
- LOGRASSO, T. A., 1992, Mat. Sci & Eng., **A155**, 115.
- MALOY, S. A., MITCHELL, T. E. and HEUER, A. H., 1994, submitted to Acta Met.
- MASSALSKI, T. B., 1990, (ed.), Binary Alloy Phase Diagrams, American Society for Metals, Metals Park, OH, 2666.
- RAO, S. I., DIMIDUK, D. M. and MENDIRATTA, M. G., 1993, Philos. Mag., **68**, 1295.
- UMAKOSHI, Y., SAKAGAMI, T., YAMANE, T. and HIRANO, T., 1989, Philos. Mag. Lett., **59**, 159.
- UMAKOSHI, Y., SAKAGAMI, HIRANO, T. and T., YAMANE, T., 1990, Acta. Met., **38**, 909.
- UNAL, O., PETROVIC, J. J., CARTER, D. H., and MITCHELL, T. E., 1990, J. Am. Ceram. Soc., **73**, 1752.

## Published papers:

Bimal K. Kad, Bernard P. Bewlay, Kenneth S. Vecchio, and Robert J. Asaro, "On the Nature of Faults in MoSi<sub>2</sub>" (1995) Philos. Mag., in press.

Bimal. K. Kad, Kenneth. S. Vecchio, Bernard. P. Bewlay and Robert. J. Asaro, "C11b -> C40 Transformation Induced 1/4<111> Faults in MoSi<sub>2</sub>" (1994) Mat. Res. Soc. Symp. Proc., **322**, 49-55.

Bimal K. Kad, Kenneth S. Vecchio, and Robert J. Asaro, "Planar Faults in Spray-Deposited MoSi<sub>2</sub>" 1993, MAS Conf. Proc., **2**, p148-149

Bimal K. Kad, Kenneth S. Vecchio and Robert J. Asaro, "Defect Structures and Planar Faults in Spray-Deposited MoSi<sub>2</sub>" 1993, Mat. Res. Soc. Symp. Proc., **288**, 1123-1128.

## B) Titanium Aluminide: microstructural development

Two areas of target development were, i) generating a physically based understanding of microstructurally sensitive mechanical response, and ii) developing processing parameters (including texture) for application specific component design. The task involved employing experimental and numerical methodologies to design optimum microstructures as well as optimum textures in these highly anisotropic materials.

Recently, an effort has been made to apply finite element procedures [Harren, Deve and Asaro, 1988], incorporating physically based crystal plasticity models [Asaro et al, 1979, 1982, 1983, 1985, 1988], to study the evolution of non-uniform deformation in TiAl based polycrystalline alloys of engineering development interest [Kad, Dao and Asaro, 1995]. The impetus for such efforts is to gather fundamental insight into microstructure sensitive deformation mechanisms, and to extract additional information, that is nominally not obtainable from traditional mechanical property measurements. The most productive approach to understanding how microstructural mechanisms operating on the grain level (i.e., in single crystals) determine the polycrystal behavior is through the development, application and the subsequent refinement of numerical procedures, which predict polycrystal response with some appropriate average of the response of its constituent grains. In lamellar TiAl alloys, such an effort is particularly desirable to help track various aspects of plastic anisotropy (Inui et al, 1992, Nakano et al, 1992) of single crystals (i.e., strength, failure strain etc.), and the contribution of micro-constituents ( $\gamma$ -grain Vs lamellar colony volume fraction) as implicit in polycrystalline aggregates (Kim, 1992). Within that framework, the results presented here are inspired by the need to explore mechanistic reasons to explain the functional dependence of ductility on  $\gamma$ -grain volume fraction in nearly lamellar alloys, figure 7(a), when no apparent clues can be discerned from the mechanical property measurements, figure 7(b). The exact details are that fully lamellar alloys exhibit very low ductility, but a significant improvement is obtained by incorporating small volume fractions of equi-axed  $\gamma$ -TiAl (occurring mostly at the lamella colony boundaries). This is a surprising and an unusual result since monolithic  $\gamma$ -TiAl is extremely brittle and exhibits fracture strains of <1%.

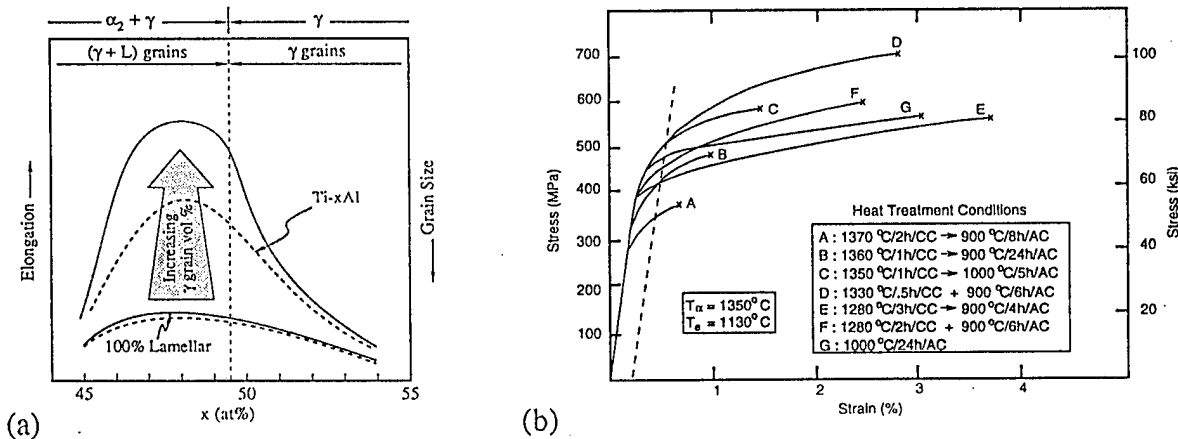


Figure 7(a) Schematic of the effects of increasing  $\gamma$  volume fraction on tensile elongation, from b) Stress-strain curves of the fully (FL) and nearly (NL) lamellar microstructures [11].

## Experimental Observations

The experimental effort is designed to supplement the existing body of experimental data especially as related to micromechanics and to provide the essential 'input' for the

quantitative efforts. This evidence is presented separately as the essential 'markers' on which the modeling effort was based, such that the theoretical results must reflect these subtleties of deformation behavior.

**Tensile failures:** Tensile failure experiments were designed to monitor the initiation and evolution of cracking during the tensile test. Fracture initiation is an important criterion for establishing the exact regions. In a typical tensile test carried out to failure, we typically end up with two fractured specimens, which only suggest the probable failure propagation path. For the sake of monitoring the evolution of fracture, we concentrate on duplex alloys since they possess a higher ductility. Tensile specimens are mechanically polished and electropolished in the gage section and the samples are strained isothermally at temperatures from RT to 500°C. Figure 8(a) shows the mixed mode fracture evidence on the surface normal to the loading direction. However, the evidence just below the fractured ends (parallel to the loading direction) indicates fractures predominantly intergranular in origin, Figure 8(b).

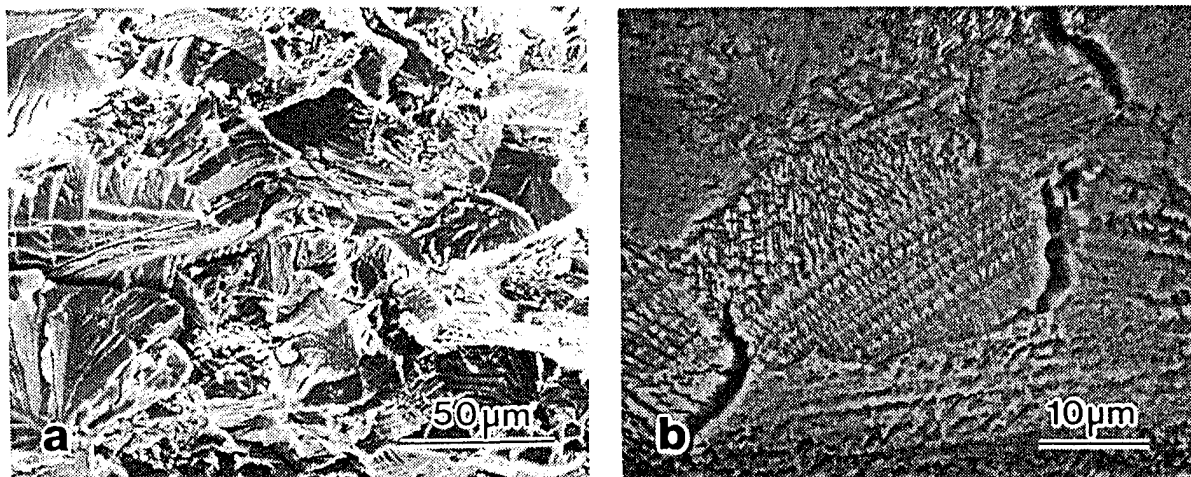


Figure 8: (a) mixed mode fracture evidence on the surface normal to the loading direction, and (b) fracture evidence just below the fractured ends (parallel to the loading direction) indicates fractures predominantly intergranular in origin.

The idea of intergranular/grain boundary cracking as being the origin of tensile failures in two phase microstructures is not currently entertained in the literature. Though a great deal of fracture evidence of failed tensile segments is presented, one can only infer the general propagation path to failure, i.e., whether intergranular or transgranular? The sites of fracture initiation (or for that matter the specific cause of failure) are not explicitly specified. It is suggested here that intergranular regions provide nucleation sites for fracture of debonding/decohesion type. Such qualitative observations in tension and in compression (described below), prior to bulk fracture, indicate that specific inhomogeneities exist in the aggregate, and consequently allow us to adapt quantitative numerical methodologies to pay specific attention to the grain boundary effects and their response to morphological variations. Looking ahead to the next section, it will be shown that the presence of large hydrostatic stresses at these boundaries provide nucleation sites for fracture due to debonding or decohesion.

**Compressive Failures:** Figure 9(a) shows the fracture evidence of a fully lamellar polycrystalline specimen (with its external surfaces prepolished) deformed  $\approx 3\%$  in compression at  $10^{-3} \text{ sec}^{-1}$  strain rate. While the bulk of the material is essentially sound, regions of microcracking and delamination are present close to the colony boundaries.

Initial experiments reveal that a significant amount of microcracking precedes bulk failure and invariably has its origins at or near the grain boundary. For example, cracks are present at  $\approx 3\%$  deformation, well before the  $\approx 18\%$  fracture strain in compression. Since compression failures are not catastrophic, their evolution is monitored readily. Observations indicate that at strains of the order of 10%, specific crystal orientations (lamellar nearly parallel to the loading direction) in the polycrystalline aggregates exhibit noticeable buckling behavior, Figure 9(b).

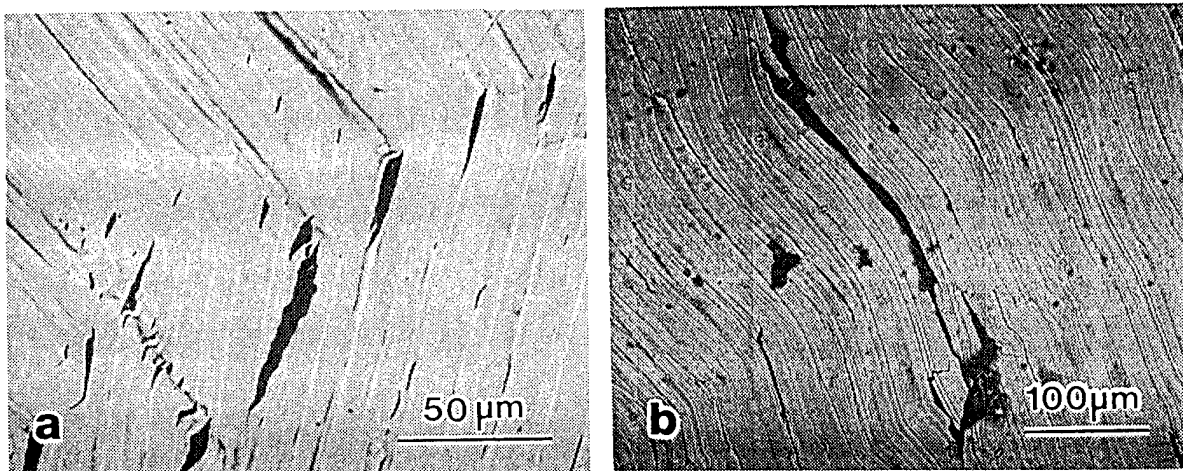


Figure 9: (a) Fracture evidence of a fully lamellar polycrystalline specimen deformed  $\approx 3\%$  in compression at  $10^{-3} \text{ sec}^{-1}$  strain rate, and (b) at  $\approx 15\%$  strain, specific crystal orientations in the polycrystalline aggregates exhibit noticeable buckling behavior.

Localized Deformations: Figure 10 shows characteristic features of localized deformations as observed in lamellar microstructures deformed 15% in compression at  $10^{-3} \text{ sec}^{-1}$  strain rate. This observation implies that homogeneous deformations, as assumed in Taylor's numerical formulation, are invalid for the constitutive study of deformation in lamellar microstructures. It is surprising that, even at relatively low strains of order of 2 to 3%, deformation is observed to be highly non-uniform. However, both the macroscopic, and

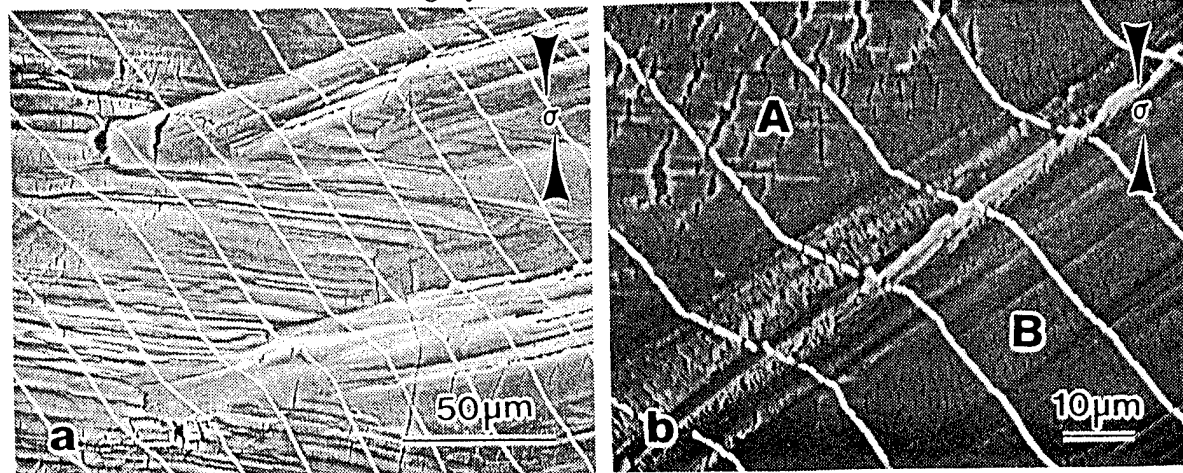


Figure 10: (a) Localized deformations, as observed by the displacement of fiducial gold lines, in lamellar microstructures. (b) Localized deformation at a bi-crystal boundary. Crystal A and B are in hard and soft mode orientations, respectively. All samples were deformed 15% in compression at  $10^{-3} \text{ sec}^{-1}$  strain rate. Arrows indicate loading direction.

the microscopic deformation behaviors in the constituent phases are highly anisotropic, thereby most likely exacerbating the non uniform deformation response.

**Interface Slip:** Figure 11(a) shows evidence of coarse slip parallel to the laminates, and specifically localized at the  $\gamma/\gamma$  and/or  $\gamma/\alpha_2$  interfaces. This observation, not only provides evidence for inhomogeneous deformation but also pinpoints the specific origin of such discontinuities. The concept of  $\gamma/\gamma$  and  $\gamma/\alpha_2$  interface sliding was introduced earlier by Kad et al.. Preliminary Ti-Ti, Ti-Al and Al-Al bonding considerations across the interfaces, following discrete partial slip vector translations, suggest that discrete slip can be accommodated at these interfaces without incurring any APB related energy penalties. Preliminary compression tests support this idea and warrant further investigation.

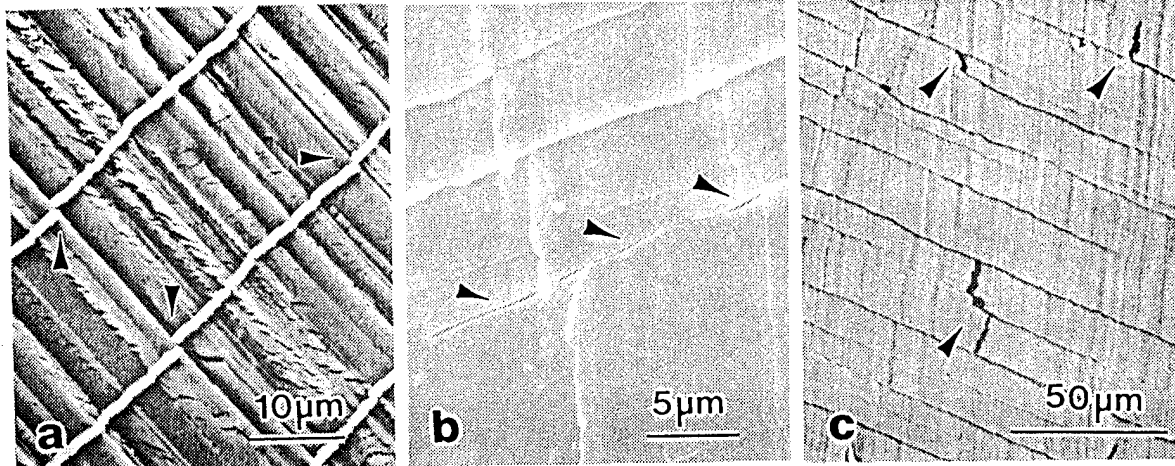


figure 11: (a) Evidence of coarse slip parallel to the laminates, localized at the  $\gamma/\gamma$  and/or  $\gamma/\alpha_2$  interfaces. (a) -> (b) transition from coarse slip to mode II cracking (arrows). (b) -> (c) transition from mode II to mixed mode with crack opening displacements (arrows) approximately parallel to the loading direction. In (b) and (c), the displacement of vertical scratches indicates the localized strain contributions for samples tested in compression.

Generally, inter-phase boundaries contain geometrical defects, ledges etc., and sliding has to be accompanied by local accommodation around the defects. This accommodation at ambient temperatures may be elastic, in which case the material response to applied stresses is instantaneous and the maximum sliding produced will be small. However, at high temperatures and high stresses, accommodation most certainly must come from matter transfer by diffusion and by dislocation movement during plastic deformation. Realistically, the behavior in the local environment of the defect is not the same as that of the grain volume. The ultimate contribution of such localized events in determining the overall creep response, at service temperatures, is of quantitative interest.

### Theoretical Results

The numerical efforts are intended to account for the plastic, crack growth and fatigue anisotropies of the lamellar crystals in the prescribed design for specific components intended for tension, compression or torsion loading or a combination thereof. The theory employed here accounts for arbitrarily large deformations and rotations, of both the material and the underlying crystalline lattice. Texture development, and the resulting anisotropic material response, are thereby accounted for along with a wide array of localized modes of deformation that are specifically important in the overall deformation behavior of TiAl lamellar microstructures as well as in the development of failure.

The reference configuration of the two dimensional fully lamellar (FL) microstructure to be analyzed is shown in Figure 12(a), where the Cartesian base vectors  $e_i$  describe the orientation of the polycrystal's reference configuration with respect to the laboratory. The finite element mesh used in the polycrystal calculations consisted initially of rectangular 'crossed-triangle' quadrilateral elements in a uniform grid 40 rectangles wide by 56 rectangles high, which is 8960 constant strain triangles totally, Figure 11(b). No geometric imperfections was present in the initial mesh. To account for the small volume fraction of  $\gamma$ -TiAl in nearly lamellar (NL) alloys, 'corner grains' were constructed comprising of 4vol%, 8vol% and 12vol%  $\gamma$ -TiAl phase located at the grain boundaries, as shown in figure 12(b).

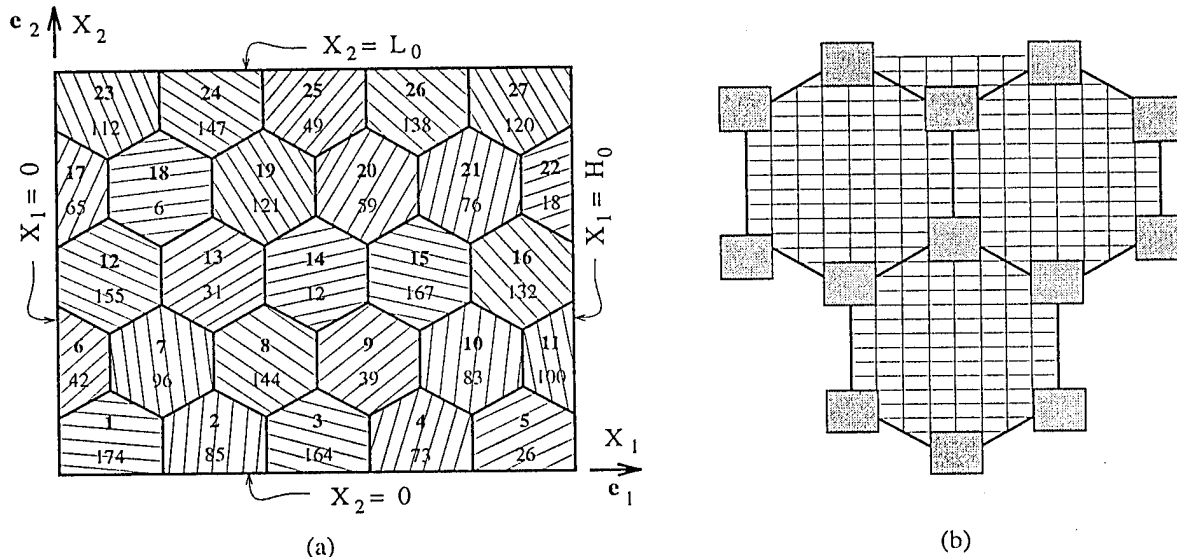


Figure 12. a) Reference configuration of the 27 lamellar crystals representing the random polycrystalline aggregate. The orientations  $\psi^n$  are selected in the  $180 \geq \psi^n \geq 0^\circ$ , and b) Incorporating small volume fractions of equi-axed  $\gamma$ -TiAl to simulate NL morphologies.

### Tensile Results

Stress-Strain Behavior: Figure 13 shows the computed stress strain behavior for the two-dimensional model microstructure, which is typical of the experimentally observed plastic behavior in lamellar microstructures, as shown in figure 7(b). Matching in the elastic regime is poor on account of the limited initial constraints in the two dimensional polycrystal, but despite the two dimensional idealization, the single crystal properties input

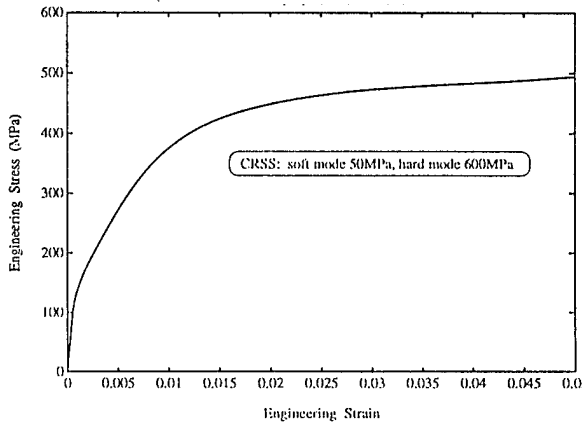
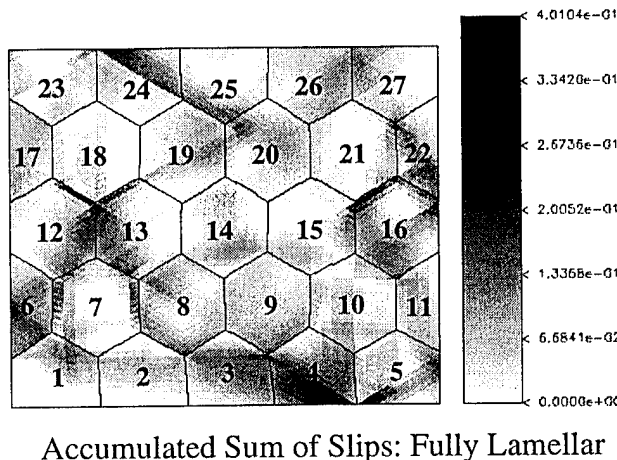


Figure 13. Computed stress-strain curve for the idealized FL microstructure of figure 12.

parameters predict the polycrystalline response with reasonable accuracy, and the underlying deformation mechanisms are well captured. Note that while the model is scale independent, these input parameters can be scaled to account for scale effects of grain size and lamella thickness changes as reported elsewhere [3].

**Strain Accumulations:** The accumulated strains at aggregate tensile strains of 2.5% is shown in figure 14. Regions of gross inhomogenous deformation, both between and within grains is immediately obvious. Maximum localized strains on the order of 40% are computed at or near the grain boundaries as illustrated between crystal pairs 1-6, 7-13, 16-21, 19-25 in figure 514(a), and experimentally observed, using fiducial displacement techniques, at bi-crystal boundaries, as shown in figure 14(b). The triple point between crystals 12, 13, and 18 constitutes strain localization of  $\approx 25\%$ . Significant inhomogeneities are also observed within the bulk of crystals 3, 4, 5, 12, 13, 16, 26, 27, with transition zones from roughly 0% strain to  $>20\%$  strain. Within a given crystal, the strain anisotropies are both parallel (in crystals 6, 8, 24) and perpendicular (in crystals 12, 13, 25, 26) to the laminates. As discussed in the next section, strain localizations parallel to the soft mode yield lower hydrostatic stress components, whereas strain localizations across the plate require activation of hard mode slip systems, or cutting of the  $\alpha_2$  plates and are considered as being additional constraining events requiring higher stress buildups.



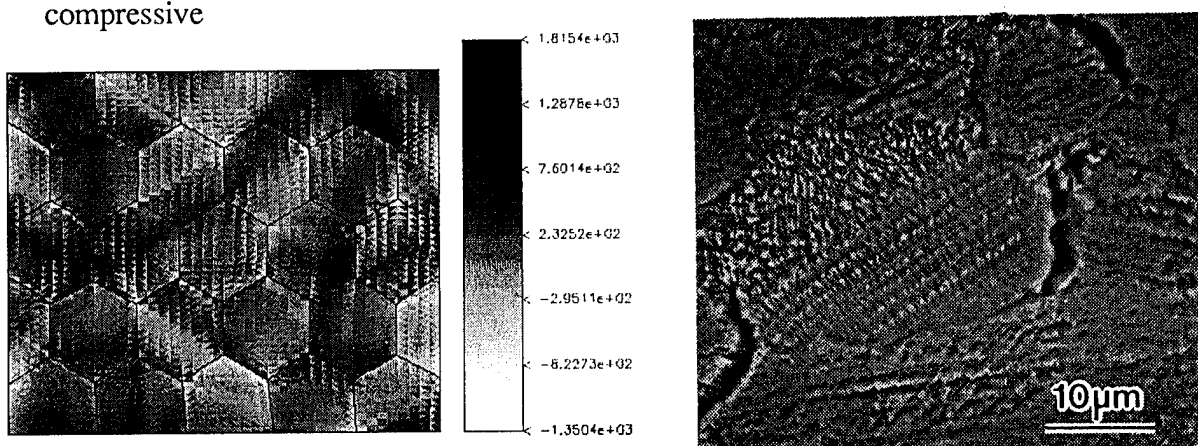
Accumulated Sum of Slips: Fully Lamellar

Figure 14. a) Theoretically computed strain accumulations (at 2.5% macroscopic strain) in FL microstructure. This strain inhomogeneity compares well with the experimentally observed strain accumulations at boundaries as shown in figure 10.

A peculiar characteristic of the crystals is their response to the varying nature of constraint at its boundaries. For example, in crystals 12, 13 (both oriented in the soft mode) large portion of the crystals do not deform as they are constrained by their neighbors. Additionally, in crystal 7, while the bulk of the crystal does not deform, some small deformations are indeed observed very close to the boundaries to comply with its more readily deformable neighbors. The orientation dependent single crystal deformation behavior is thus collectively affected by its neighbors, which in essence raises the flow stress.

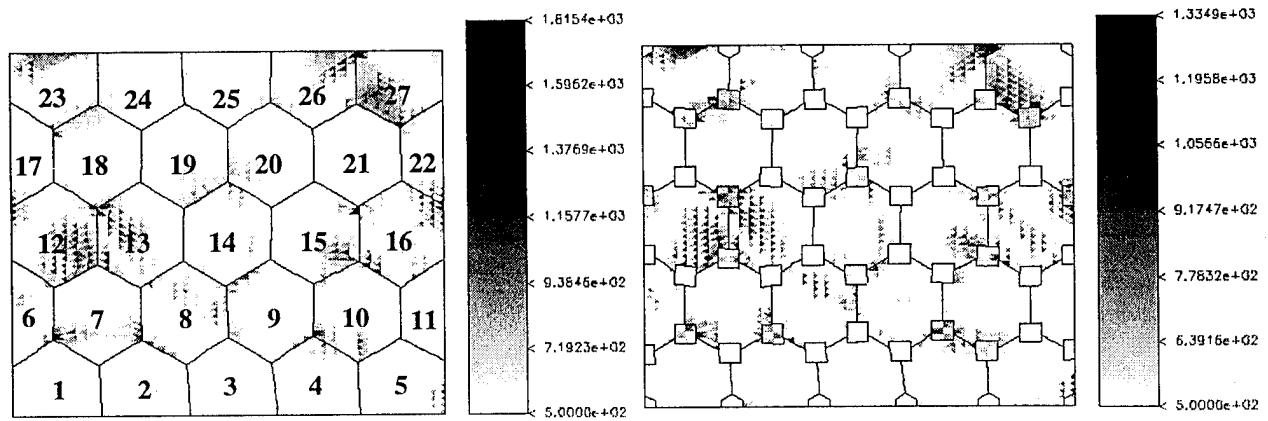
**Hydrostatic Stresses:** Hydrostatic stresses developed in the fully lamellar microstructures (corresponding to strain accumulations shown in figure 14) at 2.5% aggregate strain are shown in figure 15(a). Note that the hydrostatic stress components range from compressive to tensile. For example crystal 11 is experiencing mild compression, whereas crystal 2, 10,

27 are experiencing tension. Such fluctuations are observed as bands of tensile and compressive



(a) Hydrostatic Stress: Fully Lamellar

(b) Corresponding intergranular fracture



(c) Peak Hydrostatic Stress: Fully Lamellar

(d) Peak Hydrostatic Stress: Nearly Lamellar

Figure 15. a) Hydrostatic stress distribution in FL microstructure, b) experimental verification of the intergranular origin of fracture, c) localization of hydrostatic stresses  $>500\text{ MPa}$  near grain boundaries, and d) Peak hydrostatic stresses are significantly muted in NL microstructures.

stresses traversing through the crystals. Thus tensile/compressive bipolar states are developed also within single crystals, as seen in crystals 4, 5, 7 and 16. In particular the largest values of hydrostatic stresses, far exceeding the experimentally observed fracture stress, are encountered at the boundaries and triple points, figure 6(c) (constructed to specifically identify regions of stresses  $>500\text{ MPa}$ ). The hydrostatic stresses may arise from i) a large accumulation of strain, especially those accumulations that activate hard mode slip and ii) large deformation incompatibilities and lattice rotations between adjacent crystals, resulting in fracture initiation at the grain boundaries, as shown in Figures 8, 10 and 15(b).

Fracture evidence, just below the fractured ends, indicates fractures predominantly intergranular in origin, figure 15(b), in accord with the large hydrostatic stresses computed at the grain boundaries and triple points. Thus, it is argued that the presence of large hydrostatic stresses at these boundaries provides nucleation sites for fracture of debonding/decohesion type.

For nearly lamellar microstructures incorporating small volume fraction of equi-axed  $\gamma$ -TiAl at the boundaries, figure 15(d), we note that while the deformation substructure is

essentially similar, the peak hydrostatic stresses are progressively lower. For example they are  $\approx 1800\text{ MPa}$  in FL alloys, but down to  $\approx 1500$  (not shown) and  $\approx 1335\text{ MPa}$  in NL alloys containing 4 and 12 vol%  $\gamma$ -TiAl respectively. The arrows in figure 15(d) point specifically to sites where the benefits of  $\gamma$ -grains are realized in lowering the peak hydrostatic stresses. This effect is observed since  $\gamma$ -TiAl  $\tau_{\text{crss}}$  is less than the lamellar hard mode  $\tau_{\text{crss}}$  and acts as a soft compliant phase in mitigating the development of high stresses at the grain boundary. Grain boundary fracture is thus mitigated resulting in a more ductile alloy, in agreement with the experimental observations of figure 7(a).

### Compression Results

While tensile properties are important, primarily from an in-service design perspective, compressive mechanical behavior is also very important, particularly in deformation processing to create large shape changes. A comprehensive understanding of deformation and fracture under compressive loading in lamellar TiAl microstructures is crucial in determining the mechanical workability. The objective of our research is, therefore, to study the deformation and failure mechanisms in polycrystalline lamellar TiAl microstructures with a physically based micromechanical model. Within this framework, orientation dependent localized deformation and failure modes of poly-synthetically twinned (PST) lamellar single crystals are specifically modeled. Results are presented at large compressive strains (5 - 20% in this study).

Internal Failure Modes: In lamellar microstructures under compressive loading, intergranular fracture and internal buckling (lamellar bending) are two of the most important failure modes observed. An important type of localized mode is internal buckling. Buckling leads to large concentrated stresses which, in turn, causes the initiation of fracture. An example is shown in Figure 16(a) for a fully lamellar microstructure deformed 15% in compression. This figure contains a trace map of the lamellar orientation within each finite element throughout the microstructure. Lamellar buckling, characterized by essentially discrete kinks, is evident in grains 7, 21 and 23 whereas gross lamellar bending has occurred in grains 2, 4 and 10.

The corresponding peak hydrostatic stress contour plot, Figure 16(b) indicates that the boundary region and the buckled region develop very large hydrostatic tensile stresses under compressive global stress! Furthermore, those regions of high hydrostatic stresses inside the grains persist completely with the individual buckled grains; in fact the regions where the hydrostatic stresses are maximum have generally shifted from the grain boundary regions to within the grain matrices. This suggests a possible shift in the most likely fracture initiation sites from the grain boundaries to the grain interiors at increasing strain.

### **Summary**

Polycrystalline stress-strain behavior has been predicted, using as input the constitutive response of single crystals. The deformation is severely inhomogeneous, and deformation incompatibilities between adjacent crystals create large hydrostatic stress concentrations at grain boundaries, which are likely sites for fracture at low strains. Incorporating small volume fractions of equi-axed  $\gamma$ -TiAl, at grain boundaries, as is the case for NL microstructures, greatly reduces the magnitude of the peak hydrostatic stresses, and consequently mitigates fracture initiation. This provides a suitable explanation for the increase in ductility as associated with an increasing volume fraction of equi-axed  $\gamma$ -TiAl in lamellar microstructures. In compressive loading environments, at large strains of 10-15%, fractures initiated by internal buckling should be increasingly important.

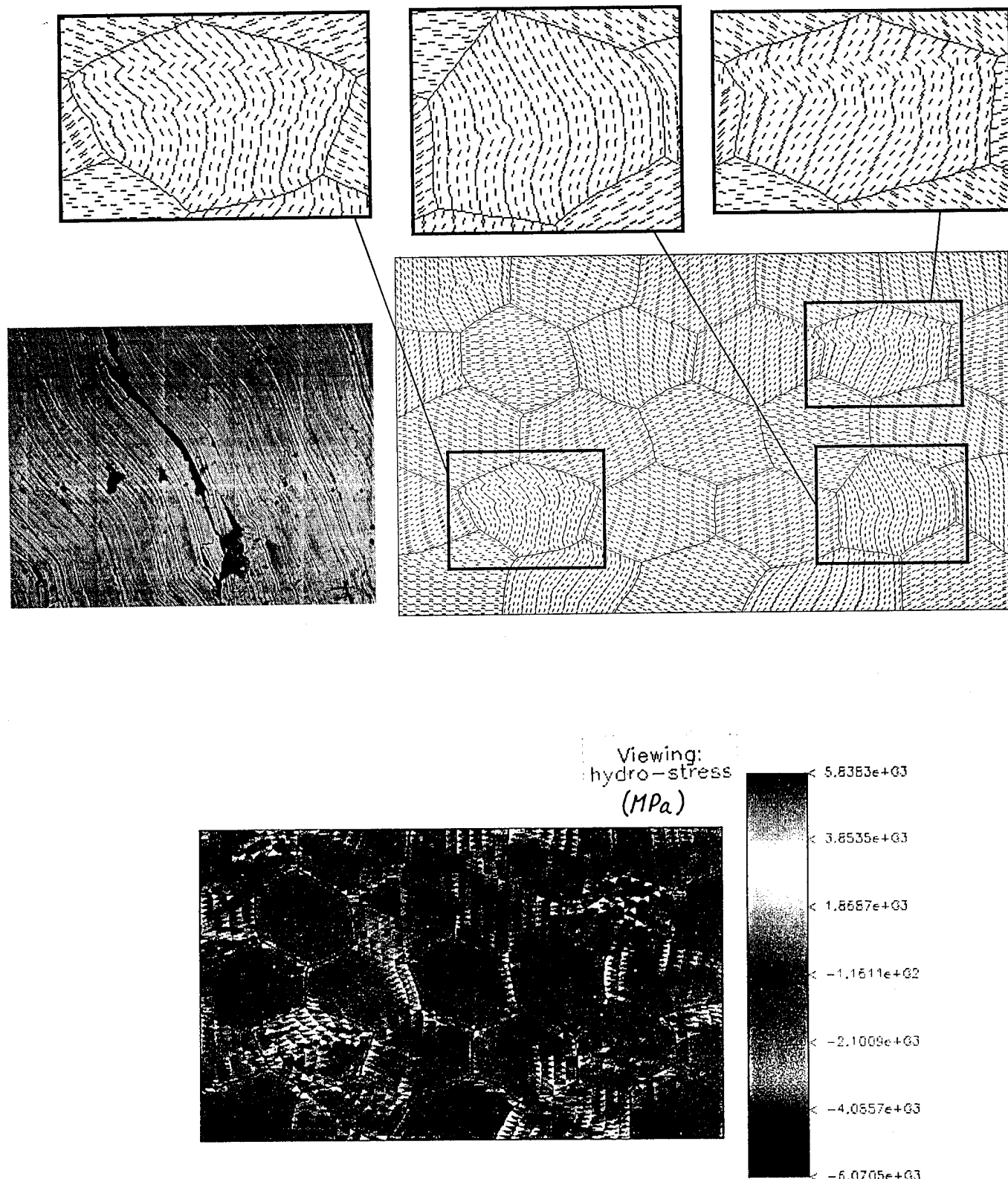


Figure 16: a) (top) Trace map of the idealized microstructure of Figure 12, deformed 15% in compression. Note that crystals with their initial lamellar orientation parallel to the loading axis, exhibit large scale buckling (in concert with experimental observations) and b) exhibit large corresponding peak hydrostatic stresses (bottom).

## References

- HARREN, S.V. DEVE, H.E., and ASARO, R.J., 1988, Acta Metall., **36**, 2435.  
 ASARO, R.J. and NEEDLEMAN, A. 1985, Acta Metall., **33** 923.  
 KAD, B.K, DAO, M. and ASARO, R.J., (1995) Philos. Mag., *in press*, Mat.Sci. & Eng., *in press*  
 ASARO, R.J., 1979, Acta Metall., **27**, 445.  
 PIERCE, D., ASARO, R.J., and NEEDLEMAN, A., 1982, Acta Met., **31** 1951.  
 McHUGH, P.E., ASARO, R.J., and SHIH, C.F., 1993 Acta Metall., **41**, 1461  
 INUI, H., OH, M.H., NAKAMURA, A, and YAMAGUCHI, M., 1992 Acta. Metall., **40**, 3095.  
 NAKANO, T., YOKOYAMA, A., and UMAKOSHI, Y., 1992 Scripta Metall., **27**, 1253  
 KIM, Y-W. Kim, 1992 Acta. Metall., **40**, 1121.

## Published papers:

Bimal K. Kad, Ming Dao and Robert J. Asaro, " Numerical Simulations of Plastic Deformation and Fracture Effects in Two Phase TiAl + Ti<sub>3</sub>Al Lamellar Microstructures" (1995) Philos. Mag., *in press*.

Bimal K. Kad, Ming Dao and Robert J. Asaro, "Numerical Simulations of Flow Stress Behavior in TiAl Based Lamellar Composites" (1995) Mater. Sci. & Eng., *in press*.

Peter M. Hazzledine and Bimal K. Kad, "Yield and Fracture of Lamellar TiAl Alloys" (1995) Mater. Sci. & Eng., *in press*.

B. J. Lee, S. Ahzi, B. K. Kad and R. J. Asaro, "On the Deformation Mechanisms in Lamellar TiAl Alloys" 1993, Scripta Met., **29**, p 823-828.

Bimal K. Kad, Ming Dao and Robert J. Asaro, " Numerical Simulations of Plastic Deformation and Fracture Effects in Two Phase TiAl + Ti<sub>3</sub>Al Lamellar Microstructures" (1994) Mat. Res. Soc. Symp. Proc., **322**, *in press*

Ming Dao, Bimal K. Kad and Robert J. Asaro, " Compressive Plastic Deformation Effects in Two Phase TiAl + Ti<sub>3</sub>Al Lamellar Microstructures" (1994) Mat. Res. Soc. Symp. Proc., **322**, *in press*

Bimal K. Kad, Peter M. Hazzledine, and Hamish L. Fraser, "On The Mechanism of Transformation of  $\gamma$ -TiAl from  $\alpha_2$ -Ti<sub>3</sub>Al" 1994, Mat. Res. Soc. Symp. Proc., **319**, 311-318.

Bimal K. Kad, Kenneth S. Vecchio, Hamish L. Fraser and Peter M. Hazzledine, "Dilatation vs Shear effects in CBED Electron Diffraction Techniques Applied to TiAl-Based Lamellar Composites" 1993, MAS Conf. Proc., **2**, 224-225.

P.M. Hazzledine, B.K. Kad and M.G. Mendiratta, "Internal Strains and Relaxations in Lamellar TiAl" 1993, Mat. Res. Soc. Symp. Proc., **308**, 725-730.

Bimal K. Kad, Peter M. Hazzledine and Hamish L. Fraser, "Lamellar Interfaces and their Contribution to Plastic Flow Anisotropy in TiAl-Based Alloys" 1993, Mat. Res. Soc. Symp. Proc., **288**, 495-500.